

Multi-wavelength characterisation of $z \sim 2$ clustered, dusty star forming galaxies discovered by *Planck*

I. Flores-Cacho^{1,2}, D. Pierini^{1,2,7}, G. Soucail^{1,3*}, L. Montier^{1,2}, H. Dole^{4,5}, E. Pointecouteau^{1,2}, R. Pelló^{1,3}, E. Le Floc'h⁶, N. Nesvadba⁴, G. Lagache^{7,4}, D. Guery⁴, and R. Cañameras⁴

(Affiliations can be found after the references)

Preprint online version: October 17, 2018

ABSTRACT

We report the discovery of PHz G95.5–61.6, a complex structure detected in emission in the *Planck* all-sky survey that corresponds to two over-densities of high-redshift (i.e., $z > 1$) galaxies. This is the first source from the *Planck* catalogue of high- z candidates (proto-clusters and lensed systems) that has been completely characterised with follow-up observations from the optical to the sub-millimetre (sub-mm) domain. *Herschel*/SPIRE observations at 250, 350 and 500 μm reveal the existence of five sources producing a 500 μm emission excess that spatially corresponds to the candidate proto-clusters discovered by *Planck*. Further observations at CFHT in the optical bands (g and i), with MegaCam, and in the near infrared (NIR) (J , H and K_s), with WIRCam, plus mid infrared (MIR) observations with IRAC/*Spitzer* (at 3.6 and 4.5 μm) confirm that the sub-mm red excess is associated with an over-density of colour-selected galaxies ($i - K_s \sim 2.3$ and $J - K \sim 0.8$ AB-mag). Follow-up spectroscopy of 13 galaxies with VLT/X-Shooter establishes the existence of two high- z structures: one at $z \simeq 1.7$ (three confirmed member galaxies), the other at $z \simeq 2.0$ (six confirmed members). The spectroscopic members of each sub-structure occupy a circular region of comoving radius smaller than 1 Mpc, which supports the existence of a physical bond among them. This double structure is also seen in the photometric redshift analysis of a sample of 127 galaxies located inside a circular region of 1'-radius containing the five *Herschel*/SPIRE sources, where we found a double-peaked excess of galaxies at $z \simeq 1.7$ and $z \simeq 2.0$ with respect to the surrounding region. These results suggest that PHz G95.5–61.6 corresponds to two accreting nodes, not physically linked to one another, embedded in the large scale structure of the Universe at $z \sim 2$ and along the same line-of-sight. In conclusion, the data, methods and results illustrated in this pilot project confirm that *Planck* data can be used to detect the emission from clustered, dusty star forming galaxies at high- z , and, thus, to pierce through the early growth of cluster-scale structures.

Key words. cosmology:observations, galaxies:high-redshift, galaxies:clusters, galaxies:clusters:individual:PHz G95.5–61.6, galaxies:star formation, large scale structure of Universe, sub-millimeter:galaxies

1. Introduction

Fully understanding the structure/galaxy formation and evolution processes that give rise to the large scale structure (LSS) and the Universe we observe today requires systematic studies of high- z galaxies, especially at $z \sim 2-3$, where the cosmic star-formation rate (SFR) density peaks (Hopkins & Beacom 2006; Sobral et al. 2013). We know that at these redshifts, during the formation of galaxy groups and clusters, there is a strong link between the star formation and black hole activities. Feedback from these two processes affects the surrounding gas, which is also heated within the deepening gravitational potential wells. However, we do not fully understand the detailed mechanisms that made the transition from the epoch of galaxy formation to the virialisation of today's massive dark matter (DM) halos (Mortonson et al. 2011). Thus, it is of crucial interest to have a complete sample of high- z proto-clusters that can be physically characterised.

Observing dusty galaxies at moderate to high redshifts was very demanding until it was realised that the Rayleigh-Jeans part of the rest-frame far-infrared (FIR) spectral energy distribution (SED) of galaxies counteracts cosmological dimming, an effect called “negative k -correction” (Blain & Longair 1993; Guiderdoni et al. 1997). As a consequence, the measured flux density of dusty galaxies at a fixed luminosity depends only weakly on redshift, allowing us to detect high- z (typically $2 <$

$z < 6$) objects in the millimetre (mm) and sub-millimetre (sub-mm) domains.

Bright high-redshift sub-mm and mm sources such as galaxy clusters/proto-clusters and gravitationally lensed galaxies are relatively rare on the sky. According to Negrello et al. (2007, 2010), the surface density of sources brighter than 300 mJy at 500 μm is 10^{-2} deg^{-2} for strongly lensed galaxies, $3 \times 10^{-2} \text{ deg}^{-2}$ for active galactic nuclei (AGN), and 10^{-1} deg^{-2} for late-type galaxies at moderate redshifts. Other models predict similar trends (e.g., Paciga et al. 2009; Lima et al. 2010; Bethermin et al. 2011; Hezaveh et al. 2012). This makes even relatively shallow sub-mm surveys interesting for searches of high- z objects, as long as they cover large parts of the sky.

Recent results from *Herschel* and the South Pole Telescope (SPT) demonstrated that sub-mm and mm observations of extragalactic sources with flux densities greater than a few hundreds of mJy at 500 μm are indeed suited to detect significant numbers of gravitationally lensed galaxies at high redshift (Greve et al. 2010; Negrello et al. 2010; Vieira et al. 2010; Combes et al. 2012; Herranz et al. 2013; Vieira et al. 2013). Other predictions (e.g., Negrello et al. 2007) indicate that many sub-Jy sub-mm sources could be high- z clusters or groups (i.e., the progenitors of today's most massive galaxy clusters), in line with the strong clustering of sub-mm galaxies or ultra-luminous infrared galaxies (ULIRGs) (Blain et al. 2004; Farrah et al. 2006; Magliocchetti et al. 2007; Viero et al. 2009; Aravena et al. 2010; Amblard et al. 2011). Most of these objects are thought to be intensely star forming (Le Floc'h et al. 2005; Caputi et al. 2007;

* Genevieve.Soucail@irap.omp.eu

Pope et al. 2008; Berta et al. 2011; Béthermin et al. 2012), in agreement with the high comoving cosmic SFR density at $z > 2$ (Hopkins & Beacom 2006; Wall et al. 2008).

In this context, the *Planck*¹ satellite (Planck Collaboration I 2011, 2014), with its full-sky coverage in the sub-mm and mm over 9 frequencies can play a key role in the systematic detection of a population of high-*z* sources. Of particular interest here is the *Planck* High Frequency Instrument (HFI, Planck Collaboration VI 2014; Planck Collaboration VII 2014; Planck Collaboration VIII 2014; Planck Collaboration IX 2014; Planck Collaboration X 2014), which has a broad wavelength coverage of 0.35–3 mm with moderate resolution (between 5 and 10 arcmin). HFI data have thus a unique potential of systematically detecting the rarest populations of bright sub-mm galaxies across the whole sky.

Indeed, using a novel method and the full sky coverage of the *Planck* survey, we have identified a sample of roughly 1300 high-*z* candidates, that are the coldest extra-galactic sources at relatively low signal-to-noise ratio (SNR) close to the confusion limit (Planck Collaboration et al. 2015a). Our unique sample complements recent efforts to detect and characterise high-*z* clusters and proto-clusters via their X-ray signature (e.g., Gobat et al. 2011; Santos et al. 2011) or via their optical properties (typically, by detecting an over-density of red galaxies and/or tracing their red sequence², with later confirmation of spectroscopic members, such as the works carried out by Gladders & Yee 2000; Stanford et al. 2012; Brodwin et al. 2012; Muzzin et al. 2013). Alternatively, targeted searches around high-*z* radio galaxies (likely to inhabit dense regions of the LSS) have also proven to be a very powerful method of detecting high-*z* (proto-) clusters (Venemans et al. 2005; Hatch et al. 2011a,b; Galametz et al. 2010, 2013; Wylezalek et al. 2013; Rigby et al. 2014). In this context, our mm/sub-mm identification of candidates using *Planck* is just the first step toward a full physical characterisation systematic follow-up observations, in order to provide constraints on a number of actively debated open questions in high-*z* research, from the dynamics of the interstellar medium (ISM) in intensely star-forming galaxies (e.g., Swinbank et al. 2011) to the mechanisms of structure formation (e.g., Mortonson et al. 2011).

A first example of such an effort is offered by Clements et al. (2014) who, combining the *Planck* Early Release Compact Source Catalog (ERCSC, Planck Collaboration VII 2011) and *Herschel* Multitiered Extragalactic Survey (HerMES, Oliver et al. 2012), selected a sample of 16 sources, four of which are confirmed structures at $0.8 \leq z \leq 2.3$. Given the selection process, the ERCSC is not ideally suited for high-*z* searches at variance from our sample of colour selected, cold sources, as shown by the high success rate (93%) of the dedicated follow-up of more than 200 of our candidates with *Herschel*/SPIRE (Planck Collaboration et al. 2015b).

This paper presents the discovery, detection and characterisation of PHz G95.5–61.6, the first proto-cluster candidate detected in emission by *Planck* and followed up photometrically at optical/NIR (CFHT), MIR *Spitzer* and FIR/sub-mm (*Herschel*) wavelengths as well as spectroscopically (VLT). This *Planck*

source is confirmed to be associated with two galaxy systems at $z \approx 1.7$ and $z \approx 2.0$. The paper is organised as follows. In Sect. 2, we give a very brief description of the *Planck* survey as well as of our method to select proto-cluster candidates that has led to the discovery of PHz G95.5–61.6. In Sect. 3, we present all the observations carried out to characterise PHz G95.5–61.6, from the sub-mm to the optical, including spectroscopy. The subsequent multi-wavelength catalogues are then described in Sect. 4. The analysis of the available follow-up observations in terms of the over-density of colour-selected galaxies is illustrated in Sect. 5, whereas the analysis in terms of photometric and spectroscopic redshifts is presented in Sect. 6. Finally, in Sects. 7 and 8, we discuss our results and provide the conclusions of this pilot study.

Throughout the paper we use a Λ CDM cosmology with $H_0 = 67.3 \text{ km s}^{-1} \text{ Mpc}^{-1}$, $\Omega_M = 0.315$ and $\Omega_\Lambda = 1 - \Omega_M$ (Planck Collaboration XVI 2014); all magnitudes are expressed in the AB system.

2. High-*z* sources in the *Planck* survey

2.1. The *Planck* survey

Planck (Tauber et al. 2010; Planck Collaboration I 2011) is the third generation space mission to measure the anisotropy of the cosmic microwave background (CMB). *Planck* observed the sky in nine frequency bands covering from 30 to 857 GHz, with high sensitivity and angular resolution from 31 to 5 arcmin. The Low Frequency Instrument (LFI; Mandolesi et al. 2010; Bersanelli et al. 2010; Mennella et al. 2011) covers the 30, 44 and 70 GHz bands with amplifiers cooled to 20 K. The High Frequency Instrument (HFI; Lamarre et al. 2010; Planck HFI Core Team 2011a) covers the 100, 143, 217, 353, 545 and 857 GHz bands with bolometers cooled to 0.1 K. Early astrophysics results, based on data taken between 13 August 2009 and 7 June 2010 (Planck HFI Core Team 2011b; Zacchei et al. 2011), are given in Planck Collaboration VIII–XXVI 2011. Our results are based on the full mission data, taken between 13 August 2009 and 14 January 2012.

2.2. Method of detection

High-*z* sources are extremely challenging to detect in the sub-mm, despite their negative *k*-correction, since they appear entangled in multiple foreground/background astrophysical emission components (such as CMB anisotropies, the cosmic infrared background – CIB – fluctuations³ or Galactic emission). Thus, it is necessary to have information in several wavelengths to extract these very cold sources from the data. *Planck*'s large wavelength coverage (from 3 mm to 350 μm) makes it ideally suited for this task.

In our quest to identify *Planck* high-*z* candidates, we used the six frequency bands of *Planck*-HFI and the IRIS version of the IRAS 100 μm map (Miville-Deschênes & Lagache 2005), restricting ourselves to only the cleanest (i.e., with minimal cirrus contamination given by a hydrogen column density of $N_{\text{HI}} < 3 \times 10^{20} \text{ cm}^{-2}$) areas of the sky. Our algorithm uses four steps, as described in full detail in Planck Collaboration et al. (2015a). First, we clean off the CMB signal in the *Planck* maps. We use the IRAS map as a template for the dust distribution to remove the Galactic cirrus contamination using the *CoCoCoDeT* algorithm (Montier et al. 2010). Then we build two

¹ *Planck* (<http://www.esa.int/Planck>) is a project of the European Space Agency (ESA) with instruments provided by two scientific consortia funded by ESA member states (in particular the lead countries France and Italy), with contributions from NASA (USA) and telescope reflectors provided by a collaboration between ESA and a scientific consortium led and funded by Denmark.

² The red sequence method is limited to $z \lesssim 1.5$.

³ See, e.g., Planck Collaboration XVIII (2011)

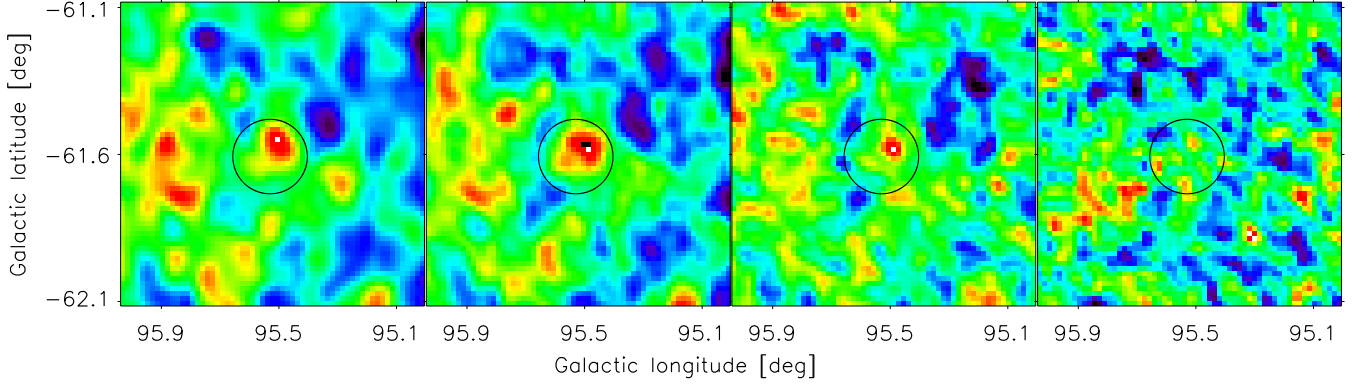


Fig. 1. From left to right: *Planck* 1 deg \times 1 deg intensity maps at 350, 550, 850 and 1380 μm (i.e., 857, 545, 353 and 217 GHz, respectively) centred on the high-*z* candidate PHz G95.5–61.6. Their individual ranges are as follows: $\pm 0.4 \text{ MJy sr}^{-1}$ (350 μm), $\pm 0.2 \text{ MJy sr}^{-1}$ (550 μm), $\pm 0.1 \text{ MJy sr}^{-1}$ (850 μm) and $\pm 0.05 \text{ MJy sr}^{-1}$ (1380 μm). In each panel, a circle with radius equal to the FWHM of the source (i.e., 7.2') is centred on the *Planck* position, measured on the sky-region with excess emission after the detection process (see Sects. 2.2 and 2.3).

excess maps (at 550 and 850 μm) defined as the difference between the *Planck* clean map and the map resulting from interpolation between neighbouring wavelengths assuming a power law. Finally, we apply an optimised mexican hat wavelet detection method to identify point sources in the excess maps.

2.3. PHz G95.5–61.6

The detection criteria previously discussed yield a sample of roughly 1300 high-*z* candidates. The true nature of each catalogue entry has to be confirmed through the photometric-redshift technique or multi-object spectroscopy. In fact, the catalogued *Planck* emission sources may correspond to a CIB over-density, a single ultra-luminous or lensed galaxy, an over-density of high-*z* dusty, star forming galaxies or a chance alignment of lower-redshift structures along the line-of-sight (i.e., a spurious detection). For a thorough discussion and characterisation of the *Planck* emission sources, we refer the interested reader to the catalogue paper (Planck Collaboration et al. 2015a).

PHz G95.5–61.6 (see Fig. 1) was selected from an earlier *Planck* internal data release as part of a pilot programme in order to be followed up with *Herschel* due to its high SNR in the excess maps. However, once compared against the final catalogue obtained from the full *Planck* data, PHz G95.5–61.6 is not an outstanding candidate, falling below the 25% top percentile of the sample in terms of flux density, colour and SNR. PHz G95.5–61.6 is partially resolved at high frequencies in the *Planck* beam, since it has a FWHM of 7.2', larger than the *Planck*-HFI FWHM of 4.7' at 550 μm . Its flux densities, as listed in the final catalogue (Planck Collaboration et al. 2015a), are: 960 ± 80 , 210 ± 70 and $1300 \pm 100 \text{ mJy}$ at 350, 550 and 850 μm , respectively. However, we make use of the original *Planck* maps (at 8' angular resolution) here.

3. Follow-up observations

3.1. *Herschel*/SPIRE

The low spatial resolution provided by the 5' beam of *Planck*/HFI between 350 and 850 μm does not enable us to distinguish the individual galaxies contributing to the detected emission at FIR/sub-mm wavelengths. Therefore, we decided to

resort to the sub-arcmin resolution offered by *Herschel*/SPIRE, which enables us to confirm the *Planck* detections, and to group our sample of high-*z* candidates according to their nature: either single sources (i.e., lensed galaxies candidates) or multiple sources (i.e., galaxy proto-clusters candidates).

In 2010 we requested (PI: Montier, Programme: OT1_lmontier_1) to follow up 10 of our candidates within the first open time period OT1. Our observations were completed between 2011 and 2013, with PHz G95.5–61.6 being the only candidate followed up in 2011.

Each SPIRE map consists of 3147 s of observations at 250, 350 and 500 μm in the 'Large Map' imaging mode. The *Herschel*/SPIRE data were reduced with the *Herschel* Interactive Processing Environment (HIPE) v8.0.3397, using the standard pipeline⁴. The final SPIRE maps are the result of direct projection onto the sky and averaging of the time-ordered data (the HIPE naive map-making routine). Their 1σ noise levels are 8.1, 6.3 and 6.8 mJy beam^{-1} at 250, 350 and 500 μm , respectively. These values are close to the confusion limits, as expected by Nguyen et al. (2010). We rely on the *Herschel* calibration⁵ of the data.

The $19' \times 19'$ maps are shown in Fig. 2. For illustration purposes, the three SPIRE images have been resampled to match the 250 μm image.

3.2. *Spitzer*/IRAC

We were granted 5 hours of observing time with *Spitzer*/IRAC (Fazio et al. 2004) for broad-band imaging (3.6 μm and 4.5 μm channels) of PHz G95.5–61.6 (plus another four high-*z* candidates), through programme 80238 (PI: Dole). We observed PHz G95.5–61.6 using a 12 point dithering pattern, with 100 s-exposure frames. This yields a total exposure of 1200 s per pixel at the centre of the field and 200–500 s per pixel at the edges. The images provided were fully reduced (level-2, post-BCDs⁶)

⁴ HIPE is a joint development by the *Herschel* Science Ground Segment Consortium, consisting of ESA, the NASA *Herschel* Science Center, and the HIFI, PACS and SPIRE consortia.

⁵ Cf. Sect. 5.2.8 of the SPIRE User Manual available at: <http://herschel.esac.esa.int/Docs/SPIRE/html/>

⁶ BCD stands for Basic Calibrated Data.

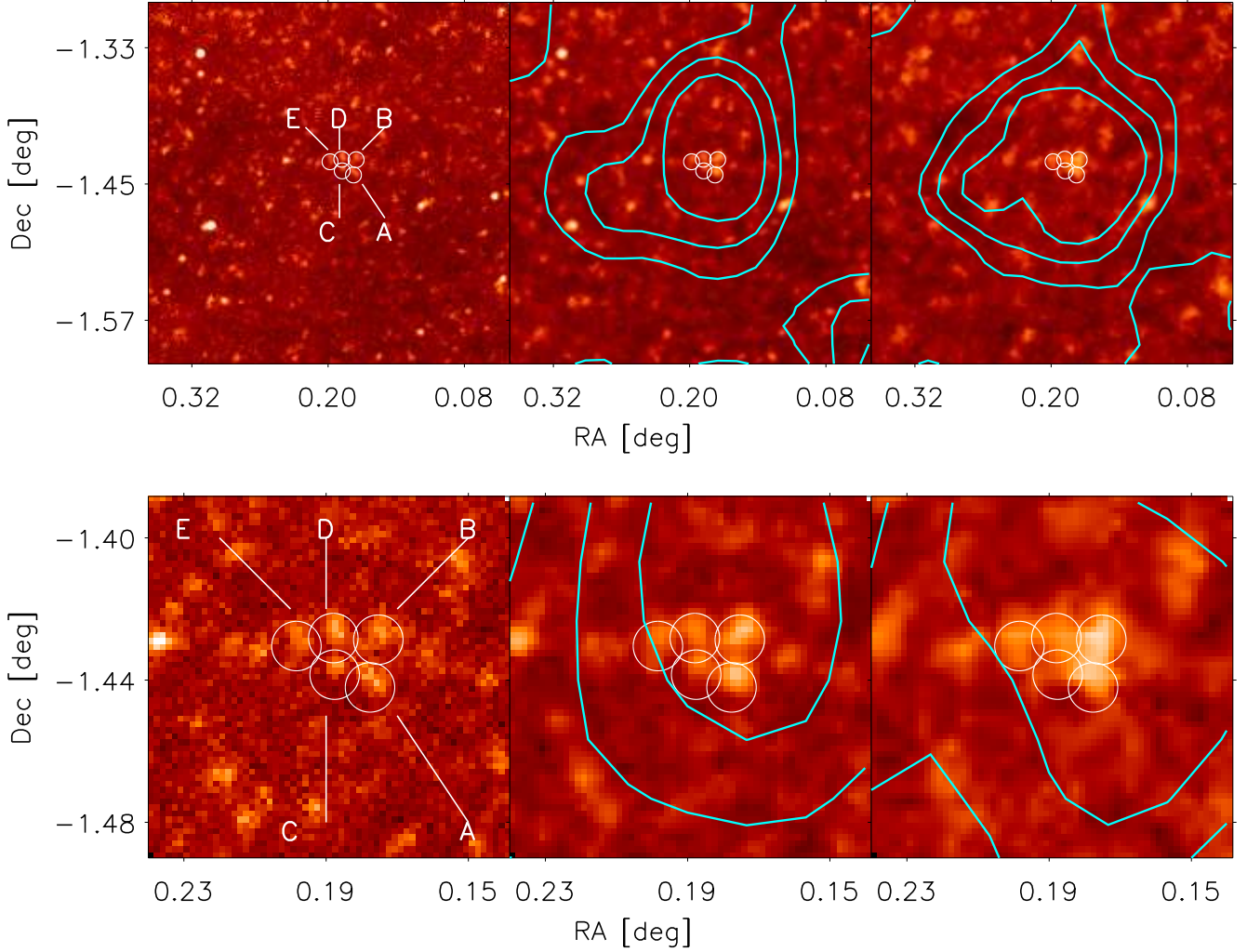


Fig. 2. *Top row:* From left to right: *Herschel*/SPIRE $19' \times 19'$ images at 250, 350 and 500 μm containing PHz G95.5–61.6. The colour scales of these maps go from 0 to 10.0 MJy sr^{-1} , 5.5 MJy sr^{-1} and 2.5 MJy sr^{-1} for 250, 350 and 500 μm , respectively. The contours of the *Planck* maps at 350 and 550 μm are over-plotted in cyan onto the SPIRE 350 and 500 μm maps, respectively. The three levels correspond to 60%, 40% and 20% of the local maximum in the *Planck* maps. The *Herschel*/SPIRE point sources within the *Planck* $\sim 5'$ beam are marked with white circles, and labelled A, B, C, D and E on the 250 μm map. *Bottom row:* A zoomed-in view into an area of $6' \times 6'$ on source. An additional level (80%) has been added to the *Planck* contours.

using the IRAC Pipeline and the MOPEX (Makovoz & Khan 2005) software, that includes sky subtraction, flat fielding, scattered light removal, flux calibration, correction for cosmetic defects (such as cosmic rays), and combining the individual AORs (Astronomical Observation Requests) to a mosaic with a pixel scale of $0.6''$. These post-BCD have 3σ limiting magnitudes of 23.3 and 23.1 for 3.6 μm and 4.5 μm , respectively. The final reduced images, centred at PHz G95.5–61.6, are shown in Fig. 3.

3.3. CFHT/WIRCam and MegaCam

For PHz G95.5–61.6, we obtained a total of 9 hours of imaging at five optical and NIR wavelengths with the wide-field cameras MegaCam (Boulade et al. 2003, - g and i bands) and WIRCam (Puget et al. 2004, - J , H and K_s bands) mounted on the Canada-France Hawaii Telescope (CFHT) through programmes 11BF11 and 11BF99 (PI: Nesvadba).

All data were obtained under good and stable atmospheric conditions with seeing $< 1.0''$ on the nights of 14 March 2012

(MegaCam) and 19 March 2012 (WIRCam). For imaging in the g and i filters, the total exposure time was 1 hour, with individual exposures of 300 s. Individual NIR frames had exposure times ranging from 15 to 59 s, resulting in a total exposure of 1 hour for K_s -band and 3 hours for H - and J -bands. All data were reduced using standard procedures in TERAPIX (Traitement Élémentaire, Réduction et Analyse des PIXELs, Bertin et al. 2002).

Our final images have 3σ limiting magnitudes (i.e., magnitude for a source with a flux SNR of 3.0, measured within an aperture of $1.9''$ -radius) equal to 25.7, 24.5, 24.3, 23.9, and 23.4 AB-mag in the g , i , J , H and K_s bands, respectively.

Out of the full coverage of 1 deg^2 and 0.13 deg^2 from MegaCam and WIRCam, respectively, we extracted square patches of $20'$ on each side, centred at the location of the *Herschel*/SPIRE sources, which were reprojected to the MegaCam pixelation ($0.186''/\text{pix}$) for the analysis with SWarp within the TERAPIX package. In Fig. 4, we show a colour-composite image of the g , i and K_s images of PHz G95.5–61.6.

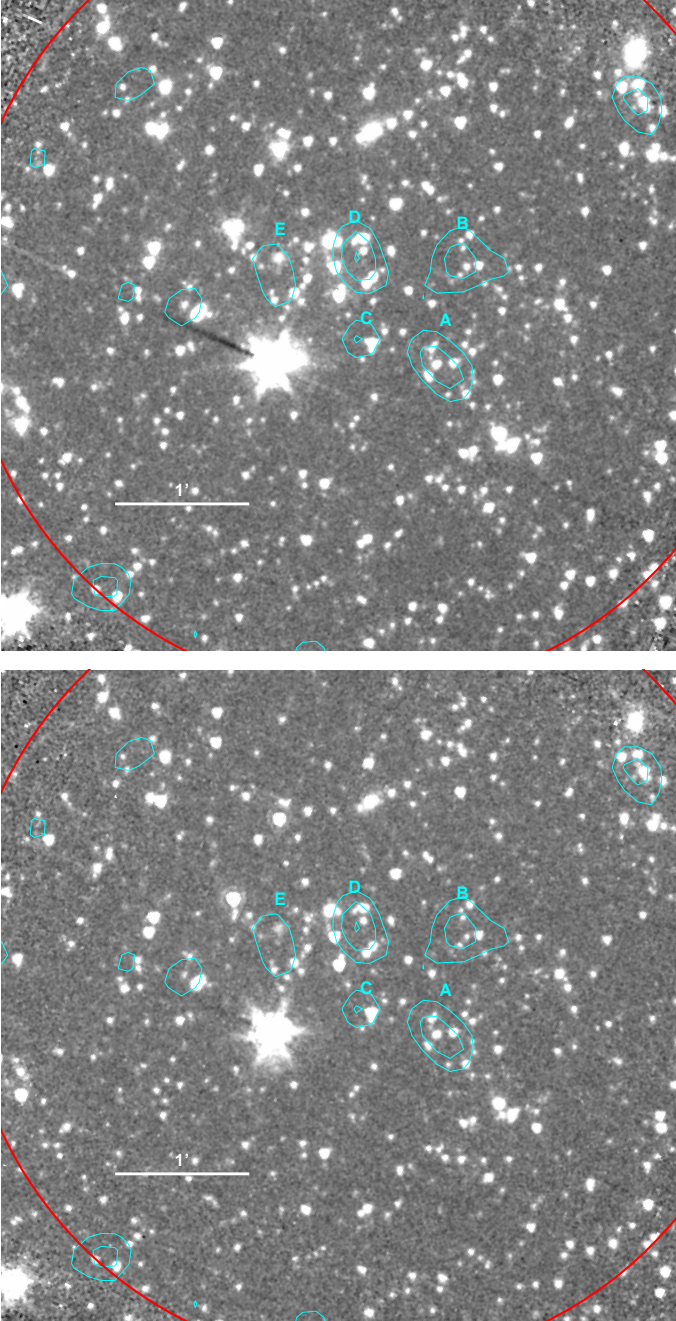


Fig. 3. IRAC 3.6 μm (top) and 4.5 μm (bottom) $5' \times 5'$ images around PHzG95.5–61.6, with the contours of the *Herschel*/SPIRE 250 μm map over-plotted in cyan. These contours correspond to deviations of 2, 3 and 4 σ . The five *Herschel*/SPIRE sources are labelled. A red circle of 3'-radius shows the deepest area, common to the two channels that we have used for the analysis. North is up, East is left.

3.4. VLT/X-Shooter

We have used 14 hours (programmes 287.A-5063 and 089.A-0276, PI: Nesvadba) of observing time with the optical/NIR Echelle spectrograph X-Shooter (Vernet et al. 2011), mounted at the VLT, in order to spectroscopically confirm the nature of PHzG95.5–61.6. We acquired long-slit spectroscopy from the ultraviolet (UV) atmospheric cutoff to the thermal cutoff at the red end of the NIR K_s band and with a spectral resolving power ~ 5000 , for 18 targets (see Sect. 6.2 for the details on the target

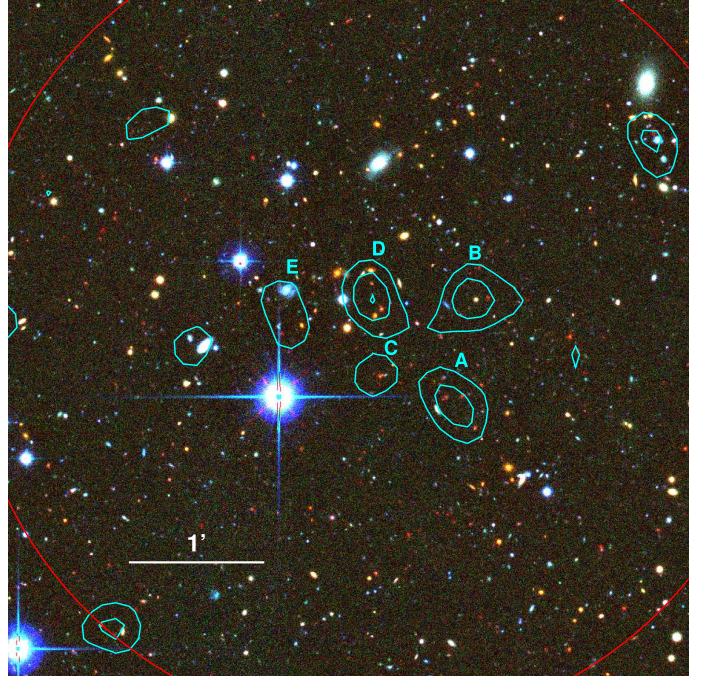


Fig. 4. False colour $5' \times 5'$ -wide image centred at PHzG95.5–61.6, with the RGB channels corresponding to K_s , i and g , respectively. The contours of the *Herschel*/SPIRE 250 μm map are over-plotted in cyan (see Fig. 3), including labels for the 5 sources in the *Planck* beam. North is up, East is left.

selection). Owing to the unique (simultaneous) spectral coverage and sensitivity of VLT/X-Shooter, various emission lines, absorption features and/or spectral breaks were expected to be detected for galaxies deemed at redshifts between 1.5 and 3.

Data were obtained in two runs, through programmes (PI: Nesvadba) 287.A-5063 (DDT) and 089.A-0276. These observations were carried out in service mode on 27–28 September 2011, and between 4 September 2012 and 12 November 2012, respectively. We used slits of 1.6'', 1.5'', and 1.2'' for the UV, optical, and NIR arms, respectively, and a 2×1 binning for the UV and optical arms. For each orientation of the slit, the total exposure was equal to 50 minutes per arm (300 s per frame), and nodding mode (source at two alternating positions along the slit, separated by roughly 5'') was chosen to ensure a good sky subtraction in the NIR. The full set of targets and slit orientations included in the two programs can be seen in Fig. 5. Atmospheric conditions were good and stable in both runs, with a seeing better than 1''.

We reduced the data with the ESO X-Shooter pipeline (Reflex-based, version 2.3.0 Modigliani et al. 2010; Freudling et al. 2013), with the physical flexure modelling of Bristow et al. (2011). One-dimensional (1-D) spectra were extracted manually, as our sources are too faint for an automatic extraction through the pipeline. We used a fixed aperture equal to the slit width to fold 2-D spectra into 1-D spectra. Possible losses of flux outside the slit were not accounted for; therefore, quantities derived from the integrated flux of spectral lines (such as the H_α -based SFRs) should be considered as lower limits. Our manually extracted 1-D spectra were then flux calibrated (using standard stars observed each night, their spectra being processed exactly the same way as for our sources), prior to the analysis.

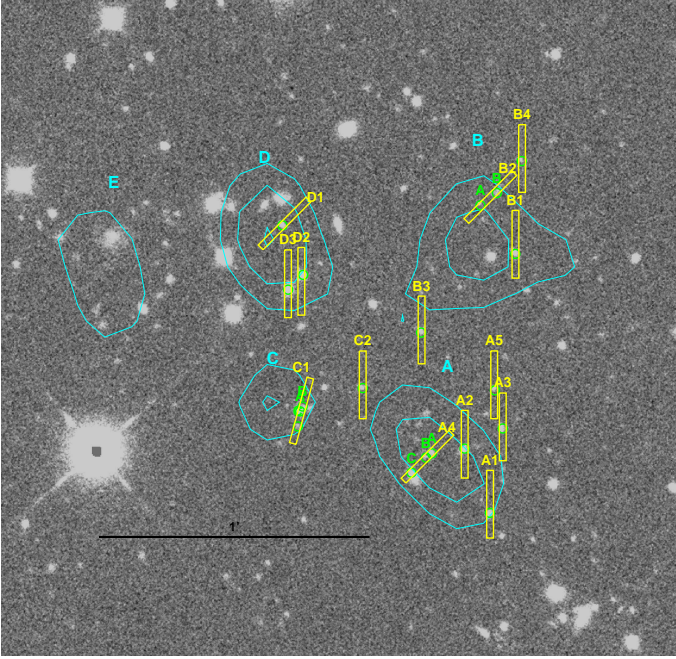


Fig. 5. Positions of the slits (yellow) used for the X-Shooter observations over-plotted onto the K_s CFHT image (grayscale). The positions of the sources are marked with green circles, and labelled where several sources fall in the same slit. The contours from the SPIRE $250\ \mu\text{m}$ image showing the FIR sources are included for reference (cyan). North is up, East is left.

For three slit orientations, we had observations from separate observing blocks (OBs), taken several days – or even a year – apart). These OBs were independently and fully reduced; the flux-calibrated 1-D spectra were then combined into a single spectrum, using the uncertainties as weights to account for the different data quality in different days⁷.

4. Optical and near infrared catalogues

4.1. Construction of a multi-wavelength source catalogue

We have built a multi-wavelength catalogue of galaxies within $5'$ from PHz G95.5–61.6 with SExtractor (Bertin & Arnouts 1996) in its double image mode, using the K_s image for detection (to favour the detection of red sources as they are more likely high-*z* objects). For the optical-NIR data from CFHT, the TERAPIX reduction already provides all the images in a common grid, which is a requirement for running SExtractor in the double image mode. However, we had to re-project the IRAC images to the K_s -image grid using SWarp (also part of the TERAPIX pipeline).

We used the standard settings for SExtractor, with a circular aperture of $1.9''$ -radius. This large aperture is due to the moderate resolution of IRAC (FWHM= $1.7''$) with respect to WIRCam (FWHM= $0.7''$). Even though the IRAC handbook⁸ establishes that the optimal aperture is $3.6''$ (and this aperture has been used in several studies, see, e.g., Laher et al. 2012), we deemed this aperture too large for our purposes, as it was prone to enclose several sources within itself. Thus, we followed the approach of Ilbert et al. (2009) for the COSMOS data, i.e., we adopted a fixed aperture radius of $1.9''$ for all bands. The ensuing aperture

⁷ Even if the atmospheric conditions were good and stable, there were differences in the SNR of the individual spectra.

⁸ See the IRAC instrument Handbook.

fluxes were corrected for the loss of flux outside the aperture, and converted into AB magnitudes using the tabulated zero-points. Finally, all magnitudes were corrected for Galactic extinction⁹ (Fitzpatrick 1999). We added an additional flag to account for nearby sources that might contaminate the aperture flux.

Since the portion of the sky imaged with IRAC (see Fig. 3) does not fully cover the circular region with a $5'$ -radius centred on the *Planck* position of PHz G95.5–61.6, we restricted the analysis to a smaller region, comprised within a source-centric distance of $3'$ (red circle in Fig. 3).

4.2. Validation of the catalogue

In order to eliminate any possible source of bias or systematics, we have completed a thorough validation of our multi-wavelength catalogue. In a first step, we compared our optical/NIR data with archival data (SDSS, 2MASS), obtaining an extremely good 1:1 correlation in all bands (the worse being J, with a median ratio between the 2MASS photometry and ours of 0.9977), within the limiting magnitudes of the archival data (and selecting only non-saturated objects in our images). This enabled us to confirm the accuracy of the zero-points below a 0.03 mag-error. In addition, to guarantee that there were no systematics in zeropoints or colours, we selected a sample of 20 isolated, non-saturated stars from the Guide Star Catalogue at CADC (Canadian Astronomy Data Centre), and fitted their SEDs with blackbody SEDs. The median deviations are all compatible with a null offset in zeropoint for all bands, within their individual dispersions.

As the sample of stars used to further validate the photometry was somewhat limited, we decided to further assess the accuracy and depths of our catalogue with a MonteCarlo (MC) approach. We injected into the final images 2000 Gaussian sources, with magnitudes ranging from 15 to 30 in all bands (fainter than the saturation level and beyond our limiting magnitudes), with a point-spread-function (PSF) matching the experimental FWHM of the images. The coordinates for the injection of these *mock* sources were randomly selected across a $20'$ patch around PHz G95.5–61.6. Then we ran SExtractor and compared recovered magnitudes with input magnitudes. This process was repeated 3 times.

Image depths (i.e., limiting magnitude) were confirmed with this MC simulation, obtaining recovery rates of 99% for magnitudes of 25.0, 23.9, 23.6, 23.4 and 22.8 AB-mag in the *g*, *i*, *J*, *H* and K_s bands, respectively. These are slightly fainter (0.1 to 0.2 mag) than our estimates based on flux, most likely due to the loss of sources falling on top of (or near to) pre-existing sources in the images.

4.3. Photometric redshift calibration

Photometric redshifts are the right tool to assess the nature of the structure(s) causing the signal detected by *Planck*. We used the BPZ code (Benitez 2000) of photo-*z* estimation. It is based on template fitting, using a multi-wavelength catalogue. In order to estimate the accuracy of the resulting photo-*z*'s, we selected seven of the 13 galaxies for which we obtained reliable redshift measurements with X-Shooter. These seven sources

⁹ We obtained the average reddening $E(B - V)$ in $2\ \text{deg}^2$ around the source from <http://irsa.ipac.caltech.edu/applications/DUST/>, using the values from Schlafly & Finkbeiner (2011), and adopted the standard visual-extinction-to-reddening ratio $A_V = 3.1E(B - V)$.

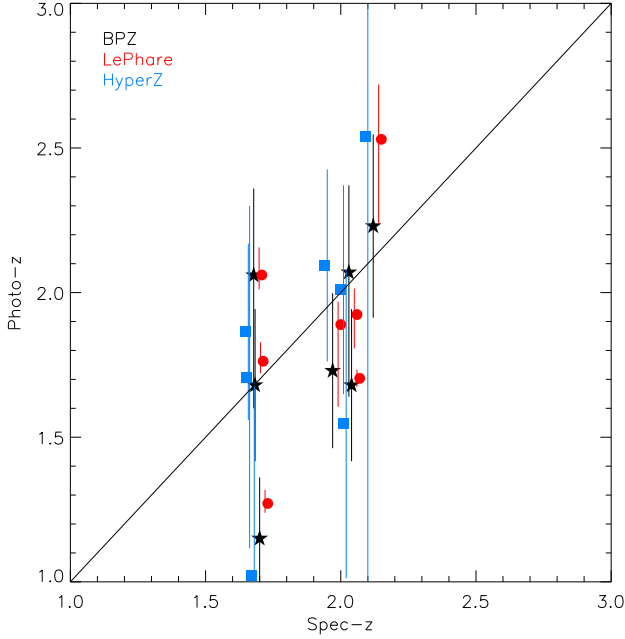


Fig. 6. Comparison of the photometric redshift estimates derived with the BPZ method of template fitting against the spectroscopic redshift obtained from X-Shooter observations. For consistency check we also used two other photo-*z* codes, namely HyperZ (Bolzonella et al. 2000) and LePhare (Arnouts et al. 1999; Ilbert et al. 2006)), which results are over-plotted. Note that they have been shifted horizontally by ± 0.03 to ease the visualisation. These two codes show similar results with slightly higher dispersion so they are not used in the rest of the paper.

have very clean photometry (neither contamination from nearby sources nor flags in the SExtractor photometry). However, our photometric redshift estimations show large uncertainties, due to broad and/or multi-peaked probability distributions in the photo-*z* space (Fig. 6). The mean dispersion (given by $\langle |z_{\text{spec}} - z_{\text{photo}}| / (1 + z_{\text{spec}}) \rangle$) is $\sim 8.5\%$, a value fully acceptable in this high redshift range, although we are fully conscious of the limitations of method even in this best-case scenario.

5. Galaxy over-density in colour

5.1. Red excess in the sub-mm

The *Planck* data for PHz G95.5–61.6 (see Fig. 1) reveal a clear excess in surface brightness at $550 \mu\text{m}$, typical of a high-*z* source, as dust emission normally peaks at $100 - 160 \mu\text{m}$ (rest-frame). From the *Herschel* images, we have extracted a catalogue with the FASTPHOT software (Bethérmin et al. 2010). Imposing a SNR threshold of 2.5 in all SPIRE bands, our catalogue comprises 28 sources within $12'$ from the image centre, out of which five are within the *Planck* beam and are labelled A, B, C, D and E in the left panel of Fig. 2. This large number of SPIRE sources clustered around the position of PHz G95.5–61.6, within the *Planck* beam, represents a deviation of 3.4σ with respect to the rest of the field in terms of the number density of SPIRE sources.

The colour-colour plot of the *Herschel*/SPIRE sources in the region of PHz G95.5–61.6 (see Fig. 7) was compared with the loci of average redshift obtained by Amblard et al. (2010) for 10^6 randomly generated SEDs. Following the prescription

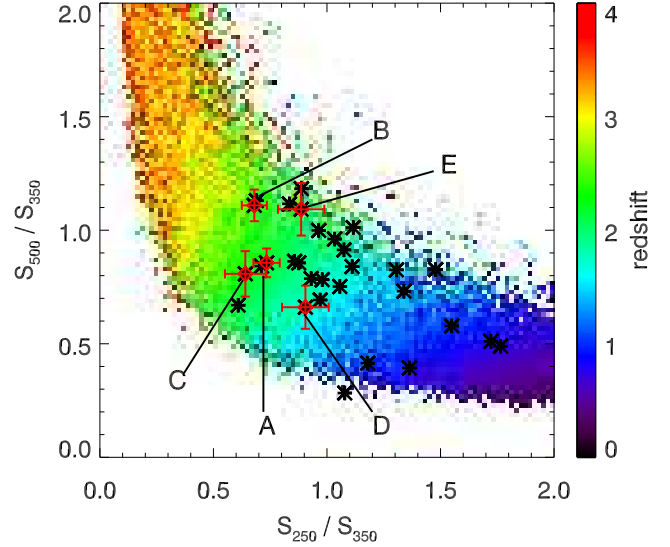


Fig. 7. Colour-colour diagram of *Herschel*/SPIRE sources in the region of PHz G95.5–61.6. The coloured background indicates the average redshift in this colour-colour space for 10^6 randomly generated synthetic SEDs (Amblard et al. 2010), modelled as modified blackbodies with dust spectral indices ranging from 1 to 2, and dust temperatures ranging from 10 K to 40 K. Sources detected above 2.5σ in all SPIRE bands are plotted as black stars. The five *Herschel*/SPIRE sources at $250 \mu\text{m}$ located around PHz G95.5–61.6, within the *Planck* beam, are marked with red diamonds and labelled A, B, C, D and E, as in Fig. 2.

of Amblard et al. (2010), these simulated SEDs correspond to modified blackbody SEDs with a spectral index ranging from 1 to 2, and dust temperature ranging from 10 K to 40 K. The five sources located within the *Planck* beam (marked with red diamonds in Fig. 7) exhibit colour-colour ratios consistent with those of $z \sim 2$ sources. This overdensity could in fact be the densest part of an even larger structure (Muldrew et al. 2015).

We have constructed a “red excess” map (M_{RX}) from the *Herschel*/SPIRE 350 and $500 \mu\text{m}$ maps (M_{350} and M_{500} , respectively) defined as:

$$M_{\text{RX}} = M_{500} - M_{350} \times \left\langle \frac{M_{500}}{M_{350}} \right\rangle_{\text{bkg}}, \quad (1)$$

where $\langle M_{500}/M_{350} \rangle_{\text{bkg}}$ is the average colour computed across the background area (defined as the region beyond the FWHM of the source flux profile measured in the *Planck* $550 \mu\text{m}$ map).

Positive fluctuations of M_{RX} trace structures with redder colours than the average value of the CIB, which can be explained by higher redshifts or colder SEDs. These “red” fluctuations may correspond to single galaxies at high redshift, clumps of coeval galaxies or alignments of faint galaxies distributed at various redshifts but along the same line-of-sight.

The SPIRE “red excess” map at $500 \mu\text{m}$ is shown in Fig. 8. We find a strong “red excess” at the position of the *Planck* source (shown as a contour map): an over-density of “red” structures in the *Herschel*/SPIRE maps is spatially correlated with PHz G95.5–61.6. However, the red excess map shows other peripheral red peaks that are not associated with our *Planck* source. We have assessed the significance of the central “red” peak against MC simulations performed on the public HerMES

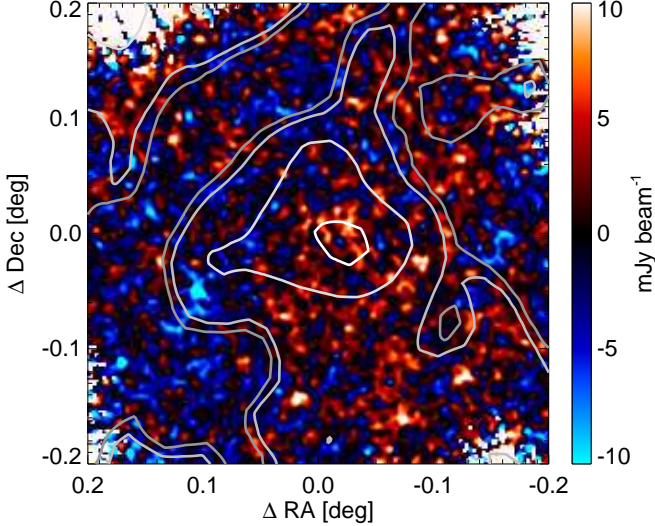


Fig. 8. SPIRE “red excess” map (M_{RX}) at $500 \mu\text{m}$. The contours of the cleaned *Planck* map at $550 \mu\text{m}$ are overlaid as grey lines at four levels: 0, 10, 50 and 90% of the local maximum.

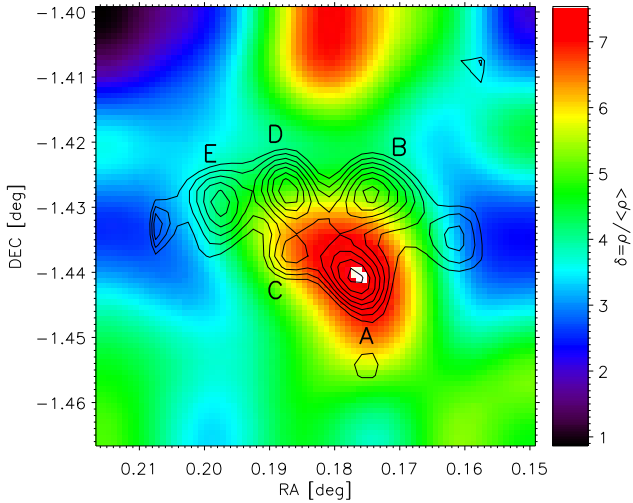


Fig. 9. Over-density maps of galaxies with colours $1.75 < i - K_s < 3.25$. The *Herschel*/*SPIRE* contours are over-plotted in black, showing the location of the *SPIRE* sources (labelled).

fields¹⁰ (HerMES Collaboration et al. 2012). The central “red excess” is significant at $\sim 2.7\sigma$. For details on the computation of this significance see Planck Collaboration et al. (2015a).

5.2. Optical and NIR over-density of red galaxies

We used the multi-wavelength photometric catalogue of galaxies built out of the CFHT and *Spitzer* imaging of PHz G95.5–61.6 to compute over-density maps of colour-selected galaxies at $1'$ -resolution. The over-density map for a given colour range is given by the ratio between the galaxy number density map and the average galaxy number density computed for this colour

¹⁰ All public HerMes data are available via the HeDaM website: <http://hedam.oamp.fr>.

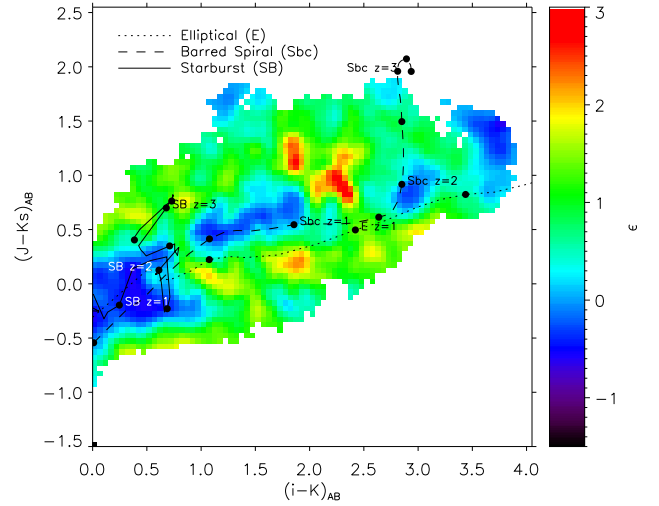


Fig. 10. Comparison of the galaxy distribution in the $i - K_s$ versus $J - K_s$ diagram for the circular region of $1'$ -radius containing the five *Herschel*/*SPIRE* sources and a region external to it (i.e., the ‘field’). An excess (ϵ , see Eq. 2) of galaxies with $i - K_s \sim 2.3$ and $J - K_s \sim 0.8$ is detected at the location of PHz G95.5–61.6 with respect to the field (see text for further details). For visualisation purposes, the map has been smoothed with a gaussian beam of two pixels. Tracks describing the colours for three typical SED templates of local galaxies, observed from $z = 0$ to $z = 4$, are over-plotted. For each track, filled black circles mark the loci at a redshift step of 0.5, with added labels at redshifts 1, 2 and 3.

interval in the field, i.e., across a square area of $15'$ on each side, masking a square area of $4'$ on each side centred on PHz G95.5–61.6. Each number density map is computed using the 10th nearest neighbour method. It reveals an over-density of (likely) high- z galaxies centred on the *Herschel*/*SPIRE* source A, which exhibits an emission peak 1.75 times higher than the average emission in the field, and represents a robust deviation (2.9σ) from the field.

When using a selection based on $i - K_s$, we clearly detect a strong over-density of galaxies with $i - K_s > 1.8$ ¹¹ centred on the *Herschel*/*SPIRE* source A (Fig. 9). The average density of such red galaxies is roughly 7 times higher than the field one (10σ deviation) near *Herschel* source A.

In addition, the distribution of galaxies in the $(J - K_s, i - K_s)$ colour-colour diagram suggests the presence of an over-density of dusty starbursts at $1 \leq z \leq 2$ (Pozzetti & Mannucci 2000; Pierini et al. 2004). To analyse the over-density of red sources around the position of PHz G95.5–61.6 in this colour-colour diagram, we have divided the colour-colour space in a regular grid with a bin of 0.05 mag and computed the number density at each pixel via the nearest-neighbour method. We have applied this method to two separate samples based on their distance to the *Herschel*/*SPIRE* sources: i) an ‘on-source’ sample that includes all sources located within $1.0'$ of PHz G95.5–61.6 and yields number density ρ_{source} ; ii) a control (or ‘field’) sample with objects within an annulus of inner and outer radii equal to $1.5'$ and $4.0'$, respectively, that yields a number density ρ_{field} . The excess

¹¹ We note that $i - K_s > 2.61$ defines Extremely Red Objects at $1 \leq z \leq 2$ (Pozzetti & Mannucci 2000)

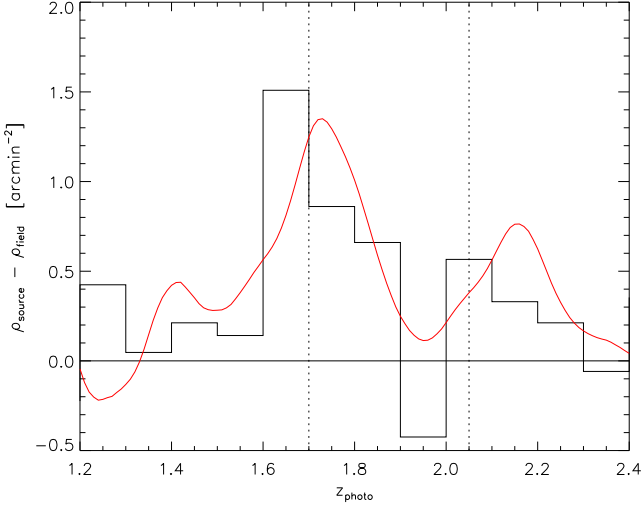


Fig. 11. Excess in the photometric redshift distribution of galaxies within $1'$ from PHz G95.5–61.6 with respect to that obtained for the rest of the field. The red line is the sum of the photometric redshift probability distribution functions for the same objects. The existence of a broad peak, consistent with the two systemic redshifts spectroscopically obtained from the X-Shooter data (vertical dashed lines) is suggested, with about 20 sources in this overdensity.

map is then given by:

$$\epsilon = \frac{\rho_{\text{source}} - \rho_{\text{field}}}{\rho_{\text{field}}}, \quad (2)$$

In Fig. 10, there is a strong excess (by 3.8 times) of colour-selected sources ($i - K_s \sim 2.35$, $J - K_s \sim 0.80$) spatially correlated with PHz G95.5–61.6. For reference, we compare this map to the tracks describing the colours obtained for three template SEDs of local galaxies observed at a redshift from 0 to 4. The elliptical galaxy template and the Sbc spiral galaxy template come from Coleman et al. (1980), whereas the starburst galaxy template comes from the Bruzual & Charlot (1993) library as described in Benítez et al. (2004). Even without any correction for dust attenuation to these redshifted tracks, the position in the colour-colour diagram of the detected excess is consistent with the presence of high- z galaxies. It also suggests that the excess is not dominated by starburst galaxies and that most of the galaxies are more standard objects, with some possible dust reddenning.

6. Redshift measurements

6.1. Photometric redshift results

We applied BPZ (Benítez 2000) to our photometric catalogue in order to obtain photometric redshifts of all sources. A library of 30 SED templates was used to reproduce the observed multi-wavelength photometry. We did not impose any prior on the data. Together with an estimation of the photometric redshift (z_{photo}), BPZ yields the redshift probability distribution function for each source, as well as a two-fold assessment of the reliability of this estimation via the χ^2 of the fit and the odds that the solution of the fit is unique.

We computed the galaxy distribution in z_{photo} (with a bin size of $\Delta z_{\text{photo}} = 0.1$) for two regions of the sky: a circular region of $1'$ -radius centred on source and its adjacent circular annulus

with outer radius of $3'$. After rescaling to the same area, we find an excess of sources at high- z around PHz G95.5–61.6 between $z_{\text{photo}} \approx 1.60$ and $z_{\text{photo}} \approx 2.20$ (Fig. 11), in good agreement with the results obtained from the galaxies observed with X-Shooter (see Sect. 6.2 below). However, given the large uncertainties in the photo- z estimations, we cannot, from these data alone, establish whether the excess of high- z galaxies is caused by two separate systems or a broad one.

6.2. Spectroscopic confirmation of the high- z nature of PHz G95.5–61.6

We obtained optical/NIR spectra of 13 targets (shown in Fig. 5, which were chosen using three general criteria:

- radial distance to one of the *Herschel*/SPIRE $250 \mu\text{m}$ sources $< 25''$;
- $K_s > 19$;
- $J - K_s \gtrsim 1$.

Specifically, these colour criteria favour the selection of galaxies with $1.0 < z_{\text{photo}} < 3.4$ when applied to the COSMOS photometric redshift catalogue¹² (Ilbert et al. 2009), consistent with our target galaxies. There are two exceptions to the colour requirement: B2b and A4c, which were simply targets of opportunity, observed by tilting the slit. In addition, C1a and C1b are fully blended in our aperture photometry.

Our observations provided reliable redshift estimations for 13 targets (listed in Table 1, with magnitudes in the optical, NIR and MIR bands), all with redshifts between ~ 1.61 and ~ 2.1 . Most of these redshift determinations arise from two or more spectral features. The exceptions are A3, A4a, A4c, and B2b, for which we reasonably assume that the brightest (single) emission line that we see is H_α .

Figure 12 shows the 2-D spectra of the sources found at the locations of the two structures, presenting the velocity offset with respect to a fixed reference frame at $z = 2.03$ and $z = 1.68$, to account for the two high- z objects. At $z \approx 2.03$, we detect H_α emission in a clear manner for D1 and C1b, and, less clearly for A4a. B2c, A4 and A3 have a faint H_α line which can be identified on the 2D spectral image. C1a shows a broad emission line (more than 200 \AA on the spectrum) and the H_α identification is confirmed by the detection of the [S II] $\lambda 6717$ - 6731 doublet. At $z \approx 1.68$, the emission from H_α is strong or clearly detected for A1, A2 and B2a.

For several galaxies, we see other lines in their spectra, including the aforementioned [N II] $\lambda 6583$ (A1, D1) and [O III] $\lambda 5007$ lines (A1, B2a, C1b, A4a) that are typical in galaxies with high star-formation rates. However, given the intrinsic faintness of our sources, most of these lines are weak and/or noisy, and are simply used for consistency check of the H_α identification. They cannot be used to further constrain the physical properties of the galaxies.

We have fitted the 1-D spectra of the galaxies associated with either structure to obtain more accurate redshift estimates. For the fit, we have adopted an educated guess of the redshift (arising from the 2-D spectrum), assumed a Gaussian profile for the H_α line plus a continuum and added, where necessary, the presence of emission coming from the [N II] $\lambda 6583$ line. This fit also allows us to estimate the flux of the H_α line, which, as discussed in Sect. 7 below, is used to derive the H_α luminosity (L_{H_α}) for each of these galaxies. The measured H_α flux should be corrected from slit-loss, as only a fraction of the source flux enters

¹² <http://irsa.ipac.caltech.edu/cgi-bin/Gator/nph-dd>

Table 1. Positions, magnitudes at optical (MegaCam), NIR (WIRCam) and MIR (IRAC) wavelengths, and spectroscopic redshifts of the 13 galaxies followed-up with VLT/X-Shooter. All magnitudes are expressed in the AB system. For clarity, the table contains three groups: members of the structure at $z \approx 1.7$, members of the structure at $z \approx 2.0$, and non-members of either group (and, in all cases, ordered from lower to higher redshift).

ID	RA	Dec	g	i	J	H	K_s	IRAC 3.6 μm	IRAC 4.5 μm	z_{spec}
A1	00:00:42.0	-01:26:40.2	24.91 ± 0.20	23.39 ± 0.15	21.94 ± 0.04	21.34 ± 0.04	20.92 ± 0.04	20.25 ± 0.04	19.99 ± 0.04	1.677
A2	00:00:42.4	-01:26:26.7	24.67 ± 0.15	23.78 ± 0.18	22.08 ± 0.05	21.33 ± 0.04	20.88 ± 0.04	20.13 ± 0.03	19.78 ± 0.03	1.684
B2a	00:00:42.1	-01:25:32.1	27.15 ± 1.44	...	22.71 ± 0.09	22.36 ± 0.09	22.35 ± 0.15	21.54 ± 0.05	21.49 ± 0.08	1.681
A3	00:00:41.8	-01:26:21.5	27.44 ± 2.00	24.01 ± 0.23	21.76 ± 0.04	21.28 ± 0.04	21.14 ± 0.05	20.69 ± 0.04	20.54 ± 0.04	2.019
A4a	00:00:42.8	-01:26:27.0	24.45 ± 0.13	23.67 ± 0.17	21.98 ± 0.05	21.44 ± 0.04	21.08 ± 0.05	20.32 ± 0.04	20.11 ± 0.04	2.032
B2c ^a	00:00:41.9	-01:25:29.3	25.43 ± 0.30	24.41 ± 0.33	22.51 ± 0.07	21.98 ± 0.06	21.70 ± 0.08	20.69 ± 0.04	20.39 ± 0.04	2.029
C1a ^b	00:00:44.8	-01:26:17.7	24.75 ± 0.16	23.16 ± 0.11	21.23 ± 0.03	20.57 ± 0.02	20.08 ± 0.03	19.25 ± 0.03	18.80 ± 0.03	2.039
C1b ^b	00:00:44.8	-01:26:16.7	24.75 ± 0.16	23.16 ± 0.11	21.23 ± 0.03	20.57 ± 0.02	20.08 ± 0.03	19.25 ± 0.03	18.80 ± 0.03	2.039
D1	00:00:45.0	-01:25:36.5	25.56 ± 0.36	24.53 ± 0.40	22.46 ± 0.07	21.78 ± 0.06	21.41 ± 0.07	20.48 ± 0.04	20.31 ± 0.04	2.018
A4c	00:00:43.1	-01:26:31.3	22.48 ± 0.03	20.97 ± 0.02	20.43 ± 0.02	20.09 ± 0.02	19.88 ± 0.02	20.08 ± 0.03	20.49 ± 0.04	1.615
A5	00:00:41.9	-01:26:13.1	24.85 ± 0.18	24.58 ± 0.40	23.50 ± 0.17	22.20 ± 0.08	22.33 ± 0.13	21.47 ± 0.05	21.36 ± 0.06	2.121
B2b ^a	00:00:41.9	-01:25:29.3	25.43 ± 0.30	24.41 ± 0.33	22.51 ± 0.07	21.98 ± 0.06	21.70 ± 0.08	20.69 ± 0.04	20.39 ± 0.04	1.921
B3	00:00:43.0	-01:26:00.3	24.12 ± 0.09	23.47 ± 0.13	22.02 ± 0.05	21.56 ± 0.04	21.23 ± 0.05	20.68 ± 0.04	20.45 ± 0.04	1.976

Table 2. Redshifts and SNR of the H_α line of the spectroscopically observed galaxies associated with the structures at $z \approx 1.7$ and $z \approx 2.0$. Redshift uncertainties are dominated by the wavelength calibration uncertainty (equivalent to ± 0.0008). The SNR values are derived from the integrated flux of the line and its uncertainty. From spectral fits, we have then obtained H_α line fluxes and luminosities, corrected from slit-loss but without any correction for extinction. For C1a, due to a broad emission line, we have large uncertainties in the fit of the H_α emission.

ID	z_{spec}	SNR	$f_{H\alpha}$ [$10^{-17} \text{erg/s/cm}^2$]	$L_{H\alpha}$ [10^{41}erg/s]
A1	1.6777	16	7.8 ± 0.5	16.3 ± 1.1
A2	1.6839	7	4.6 ± 0.6	9.8 ± 1.1
B2a	1.6819	4	2.9 ± 0.6	5.9 ± 1.3
A4a	2.0383	2	1.8 ± 0.8	5.9 ± 2.9
C1a	2.0311	4	29.1 ± 7.0	96.1 ± 23.4
C1b	2.0387	14	11.4 ± 0.8	37.9 ± 2.4
D1	2.0186	3	2.7 ± 0.8	9.0 ± 2.9

the X-shooter instrument. It is very difficult to estimate this factor for each galaxy because it strongly depends on the slit position with respect to the centroid of the source, on the seeing during the observations and on the intrinsic distribution of H_α emission and extinction within the galaxy. An estimate of this effect is proposed by Krühler et al. (2015) from a large sample of observations of GRB hosts with X-shooter: their median slit-loss factor is $1.6^{+0.7}_{-0.5}$. We decided to apply a correction factor of 1.6 to all our measures. The results are summarised in Table 2.

7. Discussion

Our analysis reveals an over-density of high- z galaxies, detected using optical/NIR colours and confirmed spectroscopically, at the location of the *Planck* high- z candidate source PHz G95.5–61.6. All the indicators used lead to the same global picture: *Planck* detected the combined emission of high- z galax-

ies (in the redshift range between 1.7 and 2.0) within a 1'-distance from this source, mostly associated with two structures.

7.1. 3D spatial distribution of the galaxies

Based on the redshift distributions we obtained, the two structures are not physically connected. It should be noted here that there is a gap in the atmospheric window in the NIR, where the atmospheric transmission is very low. This makes it difficult to spectroscopically confirm the presence of galaxies at $1.8 \leq z \leq 2.0$, and could, in principle, bias a spectroscopic study toward a double-peaked redshift distribution irrespective of the intrinsic redshift distribution. However, since we do detect two galaxies at redshifts intermediate between our two high- z structures and since the lower redshift structure is at $z \approx 1.7$ (well below the cut-off set by the atmospheric transmission) we are confident that we indeed detect two separate structures aligned along the line of sight, interpreted as two collapsing nodes across the Cosmic web. On the other hand, the galaxy members of each node do seem to be physically linked to each other and belong to the same potential well, as, in both cases, the galaxies are all encompassed within a comoving radius of $\lesssim 1.0 \text{ Mpc}$ (see Fig. 13). This size is compatible with the virial sizes of local clusters and recently discovered proto-clusters at $z > 1.5$ (e.g., Castellano et al. 2007; Andreon & Huertas-Company 2010, 2011; Gobat et al. 2013).

The fact that most of the *Herschel* sources associated with PHz G95.5–61.6 do not spatially coincide with any over-density of colour-selected galaxies in a strict sense, but are located in its outskirts, is not disturbing. In fact, studies of X-ray selected clusters at low, intermediate and high redshifts have shown that these evolved, massive DM halos can host a population of FIR/sub-mm bright sources at the boundaries of their virialized regions (Braglia et al. 2011; Santos et al. 2013) or along their matter-feeding filaments (Biviano et al. 2011). Furthermore, there is growing evidence that infalling galaxies can experience significant episodes of star-formation activity on the outskirts of clusters and, in general, along filamentary structures up to $z \approx 1$ (e.g., Porter & Raychaudhury 2007; Braglia et al. 2007; Porter et al.

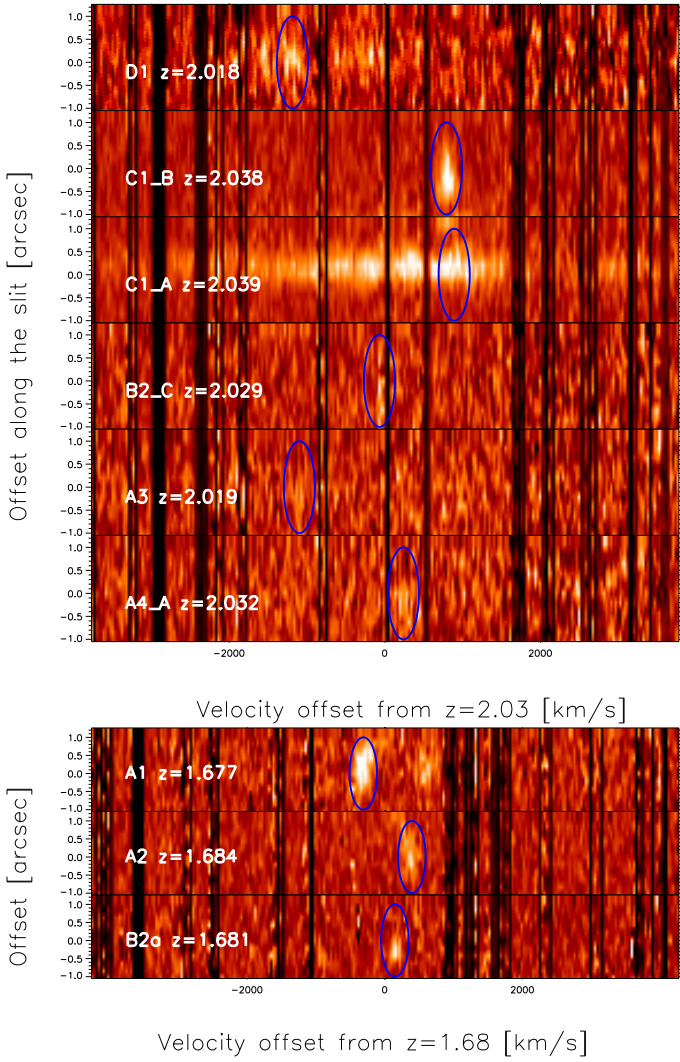


Fig. 12. Zoomed-in view to the 2-D spectra obtained with VLT/X-Shooter for those galaxies that are spectroscopically identified as members of any of the two galaxy systems set at (systemic redshift) $z \approx 2.03$ (top panel) and $z \approx 1.68$ (bottom panel). The spectra are shifted accordingly to show the velocity offset with respect to the systemic recession velocity in correspondence of the $H_\alpha \lambda 6564$ emission line, marked with a blue ellipse. For A1, and D1, the contiguous [NII] $\lambda 6584$ emission line can also be (hardly) seen. For C1a the H_α emission line is broad and blended with some contribution from the [NII] $\lambda 6550$ and $\lambda 6584$ lines, for a total width of more than 200\AA . For display purposes, known sky lines have been masked, with a width of 0.2 nm , and the colour range has been adapted for each source to maximise clarity. However, we have consistently identified the spectral features in non-masked versions of the spectra.

2008; Darvish et al. 2014). A physical explanation for this phenomenon has been recently given by Mahajan et al. (2012): according to these authors, “a relatively high galaxy density in the infall regions of clusters promotes interactions amongst galaxies, leading to momentary bursts of star formation”. The presence of a few sub-mm bright sources (each one potentially associated with just one galaxy or with a few galaxies at most) at the boundaries of the galaxy distribution in PHz G95.5–61.6 is fully consistent with the previous observational results and this new astrophysical scenario in galaxy evolution.

Table 4. Dust temperature, FIR luminosities and FIR-based SFRs for the *Herschel*/SPIRE sources within the *Planck* beam. We provide two estimations for each of these quantities assuming that all the FIR signal arises from sources either at $z = 1.7$ (top part of the table) or at $z = 2.0$ (bottom), which serve as lower and upper limits (respectively) to the expected FIR estimations.

ID	T_{dust} [K]	L_{FIR} [$10^{12} L_\odot$]	SFR [$M_\odot \text{ yr}^{-1}$]
A ($z = 1.7$)	25.9 ± 2.9	2.8 ± 0.4	482 ± 69
B ($z = 1.7$)	26.3 ± 3.0	2.7 ± 0.4	465 ± 69
C ($z = 1.7$)	32.0 ± 7.8	2.2 ± 0.8	379 ± 138
D ($z = 1.7$)	31.7 ± 7.0	2.7 ± 0.8	465 ± 138
E ($z = 1.7$)	26.4 ± 5.5	2.1 ± 0.5	362 ± 86
A ($z = 2.0$)	29.5 ± 3.5	4.3 ± 0.6	740 ± 103
B ($z = 2.0$)	29.5 ± 3.4	4.1 ± 0.5	706 ± 86
C ($z = 2.0$)	36.3 ± 9.0	3.3 ± 1.5	568 ± 258
D ($z = 2.0$)	35.9 ± 8.2	4.0 ± 1.3	689 ± 223
E ($z = 2.0$)	30.1 ± 6.7	3.1 ± 0.7	534 ± 121

7.2. Star formation rate and stellar mass

From the fitted H_α line fluxes and the measured redshifts, we have computed the H_α luminosity (L_{H_α}) and hence the SFR estimates for the galaxies that are confirmed members of the two proto-clusters, following Kennicutt (1998). Our results are summarised in Table 3. We also computed the stellar masses of these galaxies, using the relation from Daddi et al. (2004) that relies on the Ks-band magnitude. We adopted the normalisation for the SED method used by the latter authors and a Salpeter (1955) IMF. But for most of the high- z star forming galaxies it is currently admitted that dust extinction is an important factor that has a major influence on the measured H_α fluxes. To evaluate this attenuation and to correct it, we followed the results obtained by Kashino et al. (2013, 2014) on a sample of high redshift star forming galaxies (sBzK galaxies at $1.4 < z < 1.7$) detected in the COSMOS field (McCracken et al. 2010). A correlation is found between the H_α attenuation, measured spectroscopically from the H_α/H_β line ratio, and the stellar mass obtained from the BzK photometry. We used their best fit equation and applied it to our data to obtain a corrected SFR for the few galaxies for which data is available. This correcting factor is on average about 6. The majority of our galaxies shows SFRs of a few tens of $M_\odot \text{ yr}^{-1}$. Our estimations put all these galaxies below the “main sequence” part of the SFR vs stellar mass diagram (see Fig. 1 of Rodighiero et al. 2011), in agreement with the moderate optical colour we see. Hence, these galaxies represent average star forming galaxies at $z \sim 2$.

For an independent SFR estimation, we have used the *Herschel*/SPIRE data, following the same technique described in detail in Cañameras et al. (2015). We have fitted the data to a single-component modified blackbody SED (in an optically thick case scenario), obtaining a dust temperature (T_{dust}) for each source (with a fixed emissivity index $\beta = 1.6$). We have then obtained the infrared luminosities by integrating over this best-fit SED, between 8 and $1000\ \mu\text{m}$ (rest frame), and derived the SFR of each source, following Kennicutt (1998). This process is done assuming that all the SPIRE signal arises from galaxies belonging only to one of the two subsystems (either at $z = 1.7$ or at $z = 2.0$), which yields upper and lower limits on the FIR estimates of SFR. The ensuing results are listed in Table 4.

Table 3. Values for the SFR and the stellar mass obtained from direct measurement on the observed spectra and photometry of each galaxy. The specific star formation rate (sSFR) is defined as the ratio between these two quantities. The corrected SFR is deduced by applying the extinction factor $A(H_\alpha)$ line, with the relation measured in Kashino et al. (2013). C1a has been removed from the table because if is identified with a extremely red QSO so these values do not make sense. C1b is blended with C1a and K_s photometry is not reliable.

ID	z_{spec}	SFR [$M_\odot \text{ yr}^{-1}$]	M_\star^K [M_\odot]	sSFR(H_α) [yr^{-1}]	$A(H_\alpha)$ mag.	SFR _{corr} [$M_\odot \text{ yr}^{-1}$]
A1	1.6777	13.0 ± 1.0	1.7×10^{11}	7.6×10^{-11}	2.0	82 ± 6
A2	1.6839	7.8 ± 1.0	1.8×10^{11}	4.3×10^{-11}	2.0	49 ± 6
B2a	1.6819	4.6 ± 1.0	0.5×10^{11}	9.2×10^{-11}	1.4	17 ± 4
A4a	2.0383	4.8 ± 2.2	3.0×10^{11}	1.6×10^{-11}	2.3	40 ± 18
C1b	2.0387	30.1 ± 1.9				
D1	2.0186	7.2 ± 2.2	1.1×10^{11}	6.5×10^{-11}	1.8	38 ± 11

The integrated FIR-based SFR in the *Planck* beam is equal to $\sim 2000 - 3000 M_\odot \text{ yr}^{-1}$. This estimate is of same order of magnitude as the global SFR of $4924 M_\odot \text{ yr}^{-1}$ computed by Clements et al. (2014) for a proto-cluster at $z = 2.05$.

We have also fitted the broad-band SEDs of the galaxies followed up with VLT/X-Shooter to constrain their stellar masses, SFRs and bolometric dust luminosities. We have used the publicly available model package MAGPHYS¹³ (“Multi-wavelength Analysis of Galaxy Physical Properties”) that builds on the works by Bruzual & Charlot (2003); Charlot & Fall (2000). This code works in a two step process (see da Cunha et al. 2008, for a full description): 1) a library of model SEDs is assembled for a wide range of physical parameters (characterising both the stellar and interstellar components) and the redshifts and broad-band filters of the observed galaxies; and 2) a marginalised likelihood distribution is built for each physical parameter of each galaxy through comparison of the observed SED with all the synthetic ones in the library.

From this process we obtain likelihood estimations for the SFR, stellar mass, and dust luminosity. The results are listed in Table 5. We see that the SED-fitting estimates for the stellar mass (once rescaled from a Chabrier (2003) initial mass function – IMF – to a Salpeter (1955) IMF) are consistent with the estimation derived from the the K_s luminosity, with slightly lower values. The SFR derived from SED-fitting are consistent with those derived from the H_α flux, provided the dust attenuation correction if taken into account. Both values are still a factor 3 to 10 below the results obtained from the SPIRE data (Table 4) and are not easy to reconcile, although SFR derived from MAGPHYS analysis display a wide range of accepted values for some galaxies. We also remind that the SFR values obtained from the SPIRE data strongly depend on the redshift of the sources. Moreover, based on the total SFRs of each SPIRE source (see Table 4), we estimate that these sub-mm sources should have between one and three galaxy counterparts. This is consistent with the sky surface density and median SFR value of BzK -selected star forming galaxies (Daddi et al. 2004) with $1.5 \leq z \leq 2.5$ in the field that we retrieve from Oteo et al. (2014).

Finally, the stellar masses, SFRs and bolometric dust luminosities listed in Table 5 suggest that some of galaxies under study could be classified as luminous/ultra-luminous infrared

galaxies (LIRGs/ULIRGs, Daddi et al. 2005)¹⁴, and, thus, are likely responsible for a significant fraction of the fluxes of the individual SPIRE sources. In particular, the two galaxies A1 and A4a are candidate counterparts to SPIRE source A. Furthermore, the close pair C1a and C1b is a strong candidate for being associated with SPIRE source C, especially the red quasar C1a. We note that the galaxies A1, A4a, C1a, C1b and D1 are both candidate ULIRGs and spectroscopic members of either galaxy structure associated with PHz G95.5–61.6.

8. Conclusions

We combined the *Planck*/HFI and *IRAS* all-sky maps to identify the brightest, and intrinsically rarest, sub-mm emitters in the distant Universe over the cleanest 35% of the sky. We used colour-colour criteria plus flux density and signal-to-noise threshold to build a sample of several hundreds of *Planck* high-redshift candidates, amongst which we found PHz G95.5–61.6. We presented and discussed here the full characterisation of this candidate, used as the bench-mark for an ongoing follow-up programme on the full catalogue.

Our analysis shows that the excess signal detected by *Planck* for PHz G95.5–61.6 is indeed correlated with an over-density of “red sources” as seen by *Herschel*. The analysis of the optical and IR data from CFHT and *Spitzer* shows that the IR excess seen by SPIRE is caused by an excess of galaxies with typical colours of $i - K_s \sim 2.5$ and $J - K_s \sim 1.0$, consistent with being dusty, star forming galaxies at $z \sim 2$. Photometric and spectroscopic redshifts of the galaxies in the same region of the sky further support that the *Planck* detection is caused by an over-abundance of high- z galaxies. However, these galaxies are not members of a single system, but rather of two galaxy clumps viewed along the same line of sight, and located at $z \approx 1.7$ and $z \approx 2.0$.

The physical size (~ 1 Mpc) of our two proto-cluster candidates is consistent with known proto-clusters/groups at $1 \leq z \leq 2$. The star-formation rates (SFRs) of the spectroscopic members suggest that our proto-clusters host intense star formation activity, consistent with the models that predict a peak in the cosmic SFR density at $z \sim 2$.

Thus, PHz G95.5–61.6 has not only proven *Planck*'s potential for detecting high- z objects but also that the observational

¹³ MAGPHYS is maintained by E. da Cunha and S. Charlot. It is available at: <http://www.iap.fr/magphys/magphys/MAGPHYS.html>.

¹⁴ By definition, LIRGs and ULIRGs exhibit bolometric dust luminosities (from 8 to $1000 \mu\text{m}$) above 10^{11} and $[1 - 2] \times 10^{12} L_{\text{sun}}$, respectively.

Table 5. MAGPHYS 1σ confidence interval for the SFR, stellar mass, bolometric dust luminosity and sSFR derived from fitting the optical/NIR SEDs of the spectroscopic targets with the best secure redshift identification. These quantities have been obtained using the Chabrier (2003) initial mass function (IMF). To rescale them to a Salpeter (1955) IMF, an average factor of 1.4 should be applied to the SFRs and stellar masses.

ID	SFR [$M_{\odot} \text{ yr}^{-1}$]	L_{dust} [L_{\odot}]	M_{\star} [M_{\odot}]	sSFR [yr^{-1}]
A1	23.3 – 571	$(0.34 - 6.02) \times 10^{12}$	$(0.83 - 1.29) \times 10^{11}$	$(0.19 - 6.68) \times 10^{-9}$
A2	15.5 – 50	$(2.0 - 7.1) \times 10^{11}$	$(1.26 - 1.74) \times 10^{11}$	$(1.1 - 3.3) \times 10^{-10}$
B2a	1.2 – 2.8	$(1.0 - 4.0) \times 10^{10}$	$(1.8 - 2.3) \times 10^{10}$	$(0.7 - 1.5) \times 10^{-10}$
A3	2.4 – 12.9	$(0.7 - 3.1) \times 10^{11}$	$(6.8 - 7.91) \times 10^{10}$	$(0.3 - 1.7) \times 10^{-10}$
A4a	45.4 – 115.3	$(0.56 - 1.48) \times 10^{12}$	$(1.10 - 1.35) \times 10^{11}$	$(0.37 - 1.06) \times 10^{-9}$
D1	18.7 – 98.2	$(0.28 - 1.35) \times 10^{12}$	$(0.98 - 1.41) \times 10^{11}$	$(1.5 - 8.4) \times 10^{-10}$

strategy we have applied for the follow-up of these sub-mm sources is appropriate for understanding their nature.

Moreover, our results show that PLCKHZ G95.5–61.6 is a unique and extremely interesting alignment of two high-*z* proto-clusters along the line of sight (not physically linked to each other), which host an extremely vigorous star formation activity.

References

- Amblard, A., Cooray, A., Serra, P., et al. 2011, *Nature*, 470, 510
- Amblard, A., Cooray, A., Serra, P., et al. 2010, *Herschel-ATLAS: Dust temperature and redshift distribution of SPIRE and PACS detected sources using submillimetre colours*, arXiv:1005.2412
- Andreon, S. & Huertas-Company, M. 2010, *ArXiv e-prints*
- Andreon, S. & Huertas-Company, M. 2011, *A&A*, 526, A11
- Aravena, M., Younger, J. D., Fazio, G. G., et al. 2010, *ApJ*, 719, L15
- Arnouts, S., Cristiani, S., Moscardini, L., et al. 1999, *MNRAS*, 310, 540
- Benítez, N. 2000, *ApJ*, 536, 571
- Benítez, N., Ford, H., Bouwens, R., et al. 2004, *ApJS*, 150, 1
- Bersanelli, M., Mandolesi, N., Butler, R. C., et al. 2010, *A&A*, 520, A4
- Berta, S., Magnelli, B., Nordon, R., et al. 2011, *A&A*, 532, A49
- Bertin, E. & Arnouts, S. 1996, *A&AS*, 117, 393
- Bertin, E., Mellier, Y., Radovich, M., et al. 2002, in *Astronomical Society of the Pacific Conference Series*, Vol. 281, *Astronomical Data Analysis Software and Systems XI*, ed. D. A. Bohlender, D. Durand, & T. H. Handley, 228
- Bethermin, M., Dole, H., Beelen, A., & Aussel, H. 2010, *A&A*, 512, 78
- Bethermin, M., Dole, H., Lagache, G., Le Borgne, D., & Penin, A. 2011, *A&A*, 529, 4
- B  thermin, M., Le Floc’h, E., Ilbert, O., et al. 2012, *A&A*, 542, A58
- Biviano, A., Fadda, D., Durret, F., Edwards, L. O. V., & Marleau, F. 2011, *A&A*, 532, A77
- Blain, A. W., Chapman, S. C., Smail, I., & Ivison, R. 2004, *ApJ*, 611, 725
- Blain, A. W. & Longair, M. S. 1993, *MNRAS*, 264, 509
- Bolzonella, M., Miralles, J.-M., & Pell  , R. 2000, *A&A*, 363, 476
- Boulade, O., Charlot, X., Abbon, P., et al. 2003, in *Society of Photo-Optical Instrumentation Engineers (SPIE) Conference Series*, Vol. 4841, *Instrument Design and Performance for Optical/Infrared Ground-based Telescopes*, ed. M. Iye & A. F. M. Moorwood, 72–81
- Braglia, F., Pierini, D., & B  hringer, H. 2007, *A&A*, 470, 425
- Braglia, F. G., Ade, P. A. R., Bock, J. J., et al. 2011, *MNRAS*, 412, 1187
- Bristow, P., Vernet, J., & Modigliani, A. 2011, *Astronomische Nachrichten*, 332, 224
- Brodwin, M., Gonzalez, A. H., Stanford, S. A., et al. 2012, *ApJ*, 753, 162
- Bruzual, G. & Charlot, S. 2003, *MNRAS*, 344, 1000
- Bruzual, A., G. & Charlot, S. 1993, *ApJ*, 405, 538
- Ca  nemas, R., Nesvadba, N. P. H., Guery, D., et al. 2015, *A&A*, 581, A105
- Caputi, K. I., Lagache, G., Yan, L., et al. 2007, *ApJ*, 660, 97
- Castellano, M., Salimbeni, S., Trevese, D., et al. 2007, *ApJ*, 671, 1497
- Chabrier, G. 2003, *PASP*, 115, 763
- Charlot, S. & Fall, S. M. 2000, *ApJ*, 539, 718
- Clements, D. L., Braglia, F. G., Hyde, A. K., et al. 2014, *MNRAS*, 439, 1193
- Coleman, G. D., Wu, C.-C., & Weedman, D. W. 1980, *ApJS*, 43, 393
- Combes, F., Rex, M., Rawle, T. D., et al. 2012, *A&A*, 538, L4
- da Cunha, E., Charlot, S., & Elbaz, D. 2008, *MNRAS*, 388, 1595
- Daddi, E., Cimatti, A., Renzini, A., et al. 2004, *ApJ*, 617, 746
- Daddi, E., Renzini, A., Pirzkal, N., et al. 2005, *ApJ*, 626, 680
- Darvish, B., Sobral, D., Mobasher, B., et al. 2014, *ArXiv e-prints*
- Farrah, D., Lonsdale, C. J., Borys, C., et al. 2006, *ApJ*, 641, L17
- Fazio, G. G., Hora, J. L., Allen, L. E., et al. 2004, *ApJS*, 154, 10
- Fitzpatrick, E. L. 1999, *PASP*, 111, 63
- Freudling, W., Romaniello, M., Bramich, D. M., et al. 2013, *A&A*, 559, A96
- Galametz, A., Stern, D., Pentericci, L., et al. 2013, *A&A*, 559, A2
- Galametz, A., Stern, D., Stanford, S. A., et al. 2010, *A&A*, 516, A101
- Gladders, M. D. & Yee, H. K. C. 2000, *AJ*, 120, 2148
- Gobat, R., Daddi, E., Onodera, M., et al. 2011, *A&A*, 526, A133
- Gobat, R., Strazzullo, V., Daddi, E., et al. 2013, *ApJ*, 776, 9
- G  rski, K. M., Hivon, E., Banday, A. J., et al. 2005, *ApJ*, 622, 759
- Greve, T. R., Wei  , A., Walter, F., et al. 2010, *ApJ*, 719, 483
- Guiderdoni, B., Bouchet, F. R., Puget, J.-L., Lagache, G., & Hivon, E. 1997, *Nature*, 390, 257
- Hatch, N. A., De Breuck, C., Galametz, A., et al. 2011a, *MNRAS*, 410, 1537
- Hatch, N. A., Kurk, J. D., Pentericci, L., et al. 2011b, *MNRAS*, 415, 2993
- HerMES Collaboration, Oliver, S. J., Bock, J., et al. 2012, *ArXiv e-prints*
- Herranz, D., Gonz  lez-Nuevo, J., Clements, D. L., et al. 2013, *A&A*, 549, A31
- Hezaveh, Y. D., Marrone, D. P., & Holder, G. P. 2012, *ApJ*, 761, 20
- Hopkins, A. M. & Beacom, J. F. 2006, *ApJ*, 651, 142
- Ilbert, O., Arnouts, S., McCracken, H. J., et al. 2006, *A&A*, 457, 841
- Ilbert, O., Capak, P., Salvato, M., et al. 2009, *ApJ*, 690, 1236
- Kashino, D., Silverman, J. D., Rodighiero, G., et al. 2013, *ApJ*, 777, L8
- Kashino, D., Silverman, J. D., Rodighiero, G., et al. 2014, *ApJ*, 785, L37
- Kennicutt, Jr., R. C. 1998, *ARA&A*, 36, 189
- Kr  hler, T., Malesani, D., Fynbo, J. P. U., et al. 2015, *ArXiv e-prints*
- Laher, R. R., Rebull, L. M., Gorjian, V., et al. 2012, *PASP*, 124, 764
- Lamarre, J., Puget, J., Ade, P. A. R., et al. 2010, *A&A*, 520, A9
- Le Floc’h, E., Papovich, C., Dole, H., et al. 2005, *ApJ*, 632, 169
- Lima, M., Jain, B., & Devlin, M. 2010, *MNRAS*, 406, 2352
- Magliocchetti, M., Silva, L., Lapi, A., et al. 2007, *MNRAS*, 375, 1121
- Mahajan, S., Raychaudhury, S., & Pimblett, K. A. 2012, *MNRAS*, 427, 1252
- Makovoz, D. & Khan, I. 2005, in *Astronomical Society of the Pacific Conference Series*, Vol. 347, *Astronomical Data Analysis Software and Systems XIV*, ed. P. Shopbell, M. Britton, & R. Ebert, 81
- Mandolesi, N., Bersanelli, M., Butler, R. C., et al. 2010, *A&A*, 520, A3
- McCracken, H. J., Capak, P., Salvato, M., et al. 2010, *ApJ*, 708, 202
- Mennella, A., Butler, R. C., Curto, A., et al. 2011, *A&A*, 536, A3
- Miville-Desch  nes, M. & Lagache, G. 2005, *ApJS*, 157, 302
- Modigliani, A., Goldoni, P., Royer, F., et al. 2010, in *Society of Photo-Optical Instrumentation Engineers (SPIE) Conference Series*, Vol. 7737, *Society of Photo-Optical Instrumentation Engineers (SPIE) Conference Series*
- Montier, L. A., Pelkonen, V. M., Juvela, M., Ristorcelli, I., & Marshall, D. J. 2010, *A&A*, 522, 83
- Mortonson, M. J., Hu, W., & Huterer, D. 2011, *Physical Review D*, 83, 3015
- Muldrew, S. I., Hatch, N. A., & Cooke, E. A. 2015, *MNRAS*, 452, 2528
- Muzzin, A., Wilson, G., Demarco, R., et al. 2013, *ApJ*, 767, 39
- Negrello, M., Hopwood, R., De Zotti, G., et al. 2010, *Science*, 330, 800
- Negrello, M., Perrotta, F., Gonz  lez-Nuevo, J., et al. 2007, *MNRAS*, 377, 1557
- Nguyen, H. T., Schulz, B., Levenson, L., et al. 2010, *A&A*, 518, L5
- Olive, S. J., Bock, J., Altieri, B., et al. 2012, *MNRAS*, 424, 1614
- Oteo, I., Bongiovanni,   ., Magdis, G., et al. 2014, *MNRAS*, 439, 1337
- Paciga, G., Scott, D., & Chapin, E. L. 2009, *MNRAS*, 395, 1153
- Pierini, D., Maraston, C., Bender, R., & Witt, A. N. 2004, *MNRAS*, 347, 1
- Planck Collaboration, Ade, P. A. R., Aghanim, N., et al. 2015a, *ArXiv e-prints*
- Planck Collaboration, Aghanim, N., Altieri, B., et al. 2015b, *ArXiv e-prints*

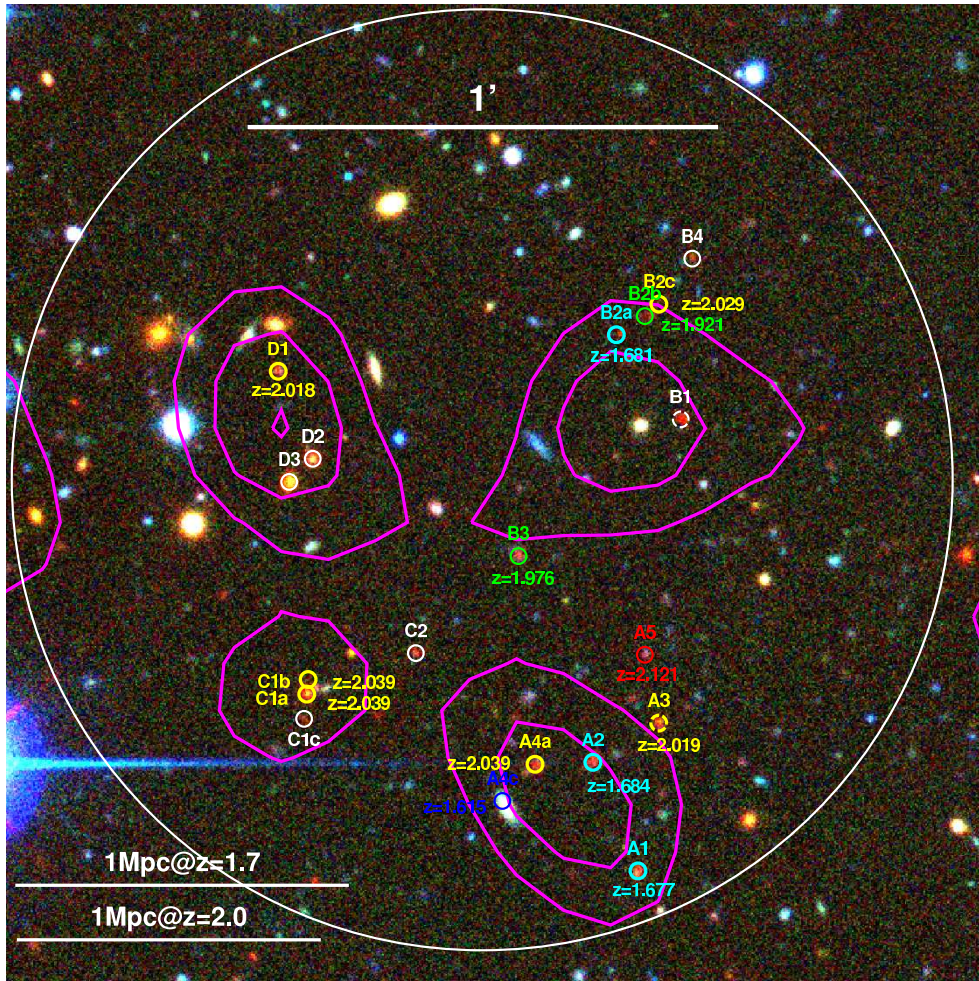


Fig. 13. Zoom-in from Fig. 4 showing the location of the spectroscopically observed galaxies. The contours of the $250\ \mu\text{m}$ *Herschel*/SPIRE map are over-plotted in magenta. These galaxies have been colour-coded according to their spectroscopic redshifts (also included in the figure), from dark blue (closest galaxy, i.e., A4c, $z = 1.615$) to red (farthest, A5, $z = 2.121$). The members of the two high- z structures are then shown in cyan ($z \approx 1.7$) and yellow ($z \approx 2.0$). The galaxies for which we could not determine their spectroscopic redshifts (B1, B4, C2, D2 and D3) are marked in white. For reference, a circle of $1'$ radius centred at RA = $00 : 00 : 43.31$ and Dec = $-01 : 25 : 50.5$ is shown in white. In addition, the scales corresponding to a comoving size of 1 Mpc at $z \approx 1.7$ and $z \approx 2.0$ are also shown in the bottom left corner. North is up and East is left.

Planck HFI Core Team. 2011a, A&A, 536, A4
 Planck HFI Core Team. 2011b, A&A, 536, A6
 Planck Collaboration I. 2011, A&A, 536, A1
 Planck Collaboration VII. 2011, A&A, 536, A7
 Planck Collaboration XVIII. 2011, A&A, 536, A18
 Planck Collaboration I. 2014, A&A, in press, arXiv:1303.5062
 Planck Collaboration VI. 2014, A&A, in press, arXiv:1303.5067
 Planck Collaboration VII. 2014, A&A, in press, arXiv:1303.5068
 Planck Collaboration VIII. 2014, A&A, in press, arXiv:1303.5069
 Planck Collaboration IX. 2014, A&A, in press, arXiv:1303.5070
 Planck Collaboration X. 2014, A&A, in press, arXiv:1303.5071
 Planck Collaboration XVI. 2014, A&A, in press, arXiv:1303.5076
 Pope, A., Chary, R. R., Alexander, D. M., et al. 2008, ApJ, 675, 1171
 Porter, S. C. & Raychaudhury, S. 2007, MNRAS, 375, 1409
 Porter, S. C., Raychaudhury, S., Pimblett, K. A., & Drinkwater, M. J. 2008, MNRAS, 388, 1152
 Pozzetti, L. & Mannucci, F. 2000, MNRAS, 317, L17
 Puget, P., Stadler, E., Doyon, R., et al. 2004, in Society of Photo-Optical Instrumentation Engineers (SPIE) Conference Series, Vol. 5492, Ground-based Instrumentation for Astronomy, ed. A. F. M. Moorwood & M. Iye, 978–987
 Rigby, E. E., Hatch, N. A., Röttgering, H. J. A., et al. 2014, MNRAS, 437, 1882
 Rodighiero, G., Daddi, E., Baronchelli, I., et al. 2011, ApJ, 739, L40
 Salpeter, E. E. 1955, ApJ, 121, 161
 Santos, J. S., Altieri, B., Popesso, P., et al. 2013, MNRAS, 433, 1287
 Santos, J. S., Fassbender, R., Nastasi, A., et al. 2011, A&A, 531, L15

Schlafly, E. F. & Finkbeiner, D. P. 2011, ApJ, 737, 103
 Sobral, D., Smail, I., Best, P. N., et al. 2013, MNRAS, 428, 1128
 Stanford, S. A., Brodwin, M., Gonzalez, A. H., et al. 2012, ApJ, 753, 164
 Swinbank, A. M., Papadopoulos, P. P., Cox, P., et al. 2011, ApJ, 742, 11
 Tauber, J. A., Mandolesi, N., Puget, J., et al. 2010, A&A, 520, A1
 Venemans, B. P., Röttgering, H. J. A., Miley, G. K., et al. 2005, A&A, 431, 793
 Vernet, J., Dekker, H., D'Odorico, S., et al. 2011, A&A, 536, A105
 Vieira, J. D., Crawford, T. M., Switzer, E. R., et al. 2010, ApJ, 719, 763
 Vieira, J. D., Marrone, D. P., Chapman, S. C., et al. 2013, Nature, 495, 344
 Viero, M. P., Ade, P. A. R., Bock, J. J., et al. 2009, ApJ, 707, 1766
 Wall, J. V., Pope, A., & Scott, D. 2008, MNRAS, 383, 435
 Wylezalek, D., Galametz, A., Stern, D., et al. 2013, ApJ, 769, 79
 Zacchei, A., Maino, D., Baccigalupi, C., et al. 2011, A&A, 536, A5

Acknowledgements. We are greatly indebted to the staff and directors of CFHT, and VLT, for their generous allocation of observing time for PHzG95.5–61.6 and spectacular help in carrying out our observations promptly and with great success. We would like to thank D. Scott, N. Welikala, M. Béthermin, M. Limousin and M. Polletta for their helpful input discussing this work. We would like to thank the anonymous referee for useful comments and suggestions that helped to improve the quality of this paper.

A description of the Planck Collaboration and a list of its members can be found at [the ESA website](#). The development of *Planck* has been supported by: ESA; CNES and CNRS/INSU-IN2P3-INP (France); ASI, CNR, and INAF (Italy);

NASA and DoE (USA); STFC and UKSA (UK); CSIC, MICINN and JA (Spain); Tekes, AoF and CSC (Finland); DLR and MPG (Germany); CSA (Canada); DTU Space (Denmark); SER/SSO (Switzerland); RCN (Norway); SFI (Ireland); FCT/MCTES (Portugal); and DEISA (EU). The Herschel spacecraft was designed, built, tested, and launched under a contract to ESA managed by the *Herschel/Planck* Project team by an industrial consortium under the overall responsibility of the prime contractor Thales Alenia Space (Cannes), and including Astrium (Friedrichshafen) responsible for the payload module and for system testing at spacecraft level, Thales Alenia Space (Turin) responsible for the service module, and Astrium (Toulouse) responsible for the telescope, with in excess of a hundred subcontractors. This work is based in part on observations made with the Spitzer Space Telescope, which is operated by the Jet Propulsion Laboratory, California Institute of Technology under a contract with NASA. Based on observations obtained at the Canada-France-Hawaii Telescope (CFHT) which is operated by the National Research Council of Canada, the Institut National des Sciences de l'Univers of the Centre National de la Recherche Scientifique of France, and the University of Hawaii. Based on observations made with ESO Telescopes at the La Silla Paranal Observatory under programme IDs 287.A-5063 and 089.A-0276.

IFC, LM and EP acknowledge the support from grant ANR-11-BS56-015. DP acknowledges the financial support from Labex OCEVU. This work has been carried out thanks to the support of the OCEVU Labex (ANR-11-LABX-0060) and the A*MIDEX project (ANR-11-IDEX-0001-02) funded by the "Investissements d'Avenir" French government program managed by the ANR. We acknowledge the use of the HEALPix software (Górski et al. 2005).

-
- ¹ Université de Toulouse, UPS Toulouse III - OMP, IRAP, Toulouse, France
 - ² CNRS, IRAP, Institut de Recherche en Astrophysique et Planétologie, 9 Avenue du Colonel Roche, BP 44346, F-31028 Toulouse cedex 4, France
 - ³ CNRS, IRAP, 14 Avenue Edouard Belin, F-31400 Toulouse, France
 - ⁴ Institut d'Astrophysique Spatiale, CNRS (UMR8617) Université Paris-Sud 11, Bâtiment 121, Orsay, France
 - ⁵ Institut Universitaire de France, 103 bd Saint-Michel, F-75005, Paris, France
 - ⁶ Laboratoire AIM, IRFU/Service d'Astrophysique - CEA/DSM - CNRS - Université Paris Diderot, Bât. 709, CEA-Saclay, F-91191 Gif-sur-Yvette Cedex, France
 - ⁷ Aix Marseille Université, CNRS, LAM (Laboratoire d'Astrophysique de Marseille) UMR 7326, 38 rue Frédéric Joliot-Curie, F-13388 Marseille cedex 13, France